International Journal of Solids and Structures 166 (2019) 183–196

Contents lists available at ScienceDirect

International Journal of Solids and Structures

journal homepage: www.elsevier.com/locate/ijsolstr

Phase field modeling of heterogeneous microcrystalline ceramics

J.D. Clayton[a,b,*], R.B. Leavy[a], J. Knap[c]

[a] Impact Physics, US ARL, Aberdeen, MD 21005, USA
[b] A. James Clark School of Engineering, University of Maryland, College Park, MD 20742, USA
[c] Computational and Engineering Sciences, US ARL, Aberdeen, MD 21005, USA

ARTICLE INFO

Article history:
Received 22 December 2018
Revised 19 February 2019
Available online 23 February 2019

Keywords:
Ceramics
Elasticity
Fracture
Twinning
Plasticity
Phase field

ABSTRACT

Diffuse interface models and simulations capture deformation and failure of polycrystalline ceramics with multiple phases. Two heterogeneous ceramic solids are investigated. The first consists of a boron carbide matrix phase embedded with titanium diboride grains. Boron carbide may undergo cleavage fracture, twinning, and amorphization under sufficient mechanical loading. Titanium diboride demonstrates cleavage fracture and limited plastic slip. The second ceramic composite consists of diamond crystals with a smaller fraction of silicon carbide grains, where the latter may encapsulate the former in a micro- or nano-crystalline matrix and/or may be interspersed as larger micro-crystals among the diamond grains. Diamond may undergo cleavage fracture while the cubic phase of silicon carbide may fracture and twin. A general constitutive framework suitable for representing behaviors of all phases of each material system is reported. This phase field framework is implemented in three-dimensional (3D) finite element (FE) simulations of polycrystalline aggregates under compressive loading. Numerical results demonstrate effects of grain and phase morphology and activation or suppression of slip or twinning mechanisms on the overall strength and ductility of each material system. Efforts to inhibit localization and cleavage in boron carbide crystals, including addition of titanium diboride, promote increases in strength of the first composite, though residual stresses may be necessary to realize toughness improvements observed experimentally. In the second composite, layers of softer silicon carbide nanocrystals along grain boundaries (GBs) improve overall strength and ductility relative to addition of larger bulk silicon carbide grains.

Published by Elsevier Ltd.

1. Introduction

Crystalline ceramics are important in technological applications requiring materials with high hardness, high stiffness, strong wear resistance, and relatively low mass density. Overall strength of these solids is often compromised by relatively low ductility and low fracture toughness. Depending on crystal type and microstructure, ceramics subjected to mechanical loading may demonstrate various deformation mechanisms in addition to elastic deformation and fracture; these may include limited dislocation glide with stacking fault creation, deformation twinning, and solid-solid phase changes. Such latter inelastic mechanisms are categorized generally here as “structural transformations.”

Theoretical and numerical methods for representing behavior of polycrystalline solids undergoing one or more such mechanisms include traditional continuum models with internal state variables (Espinosa, 1995; Bammann and Solanki, 2010; Clayton and Tonge, 2015), cohesive models of fracture (Xu and Needleman, 1994; Tomar et al., 2004; Clayton, 2005; Tomar, 2008), material point methods for fracture (Bardenhagen et al., 2011), and diffuse interface methods such as phase field models for structural transformations (Clayton and Knap, 2011a; Levin et al., 2013; Levitas, 2014) as well as fracture (Borden et al., 2012; Clayton and Knap, 2014; 2016). A novel approach combining elements of phase field theory and Finsler differential geometry (Clayton, 2017b,c) has recently been implemented in 3D FE simulations of structural transformations and fracture of ceramic polycrystals (Clayton and Knap, 2018a,b).

The current work invokes phase field theory. Advantages of the method include the following: relatively few material parameters are needed with little or no calibration, gradients of order parameters entering the energy functional enable regularized numerical solutions, and conventional continuum FE meshes can be used, without need for resolution of sharp interfaces, element deletion, or explicit mesh separation. The aforementioned differential-geometric framework essentially enriches phase field theory by enabling dependence of lengths and volumes of material

* Corresponding author at: PLXODRDRL-WMP-C, Aberdeen Proving Ground, PLXOSMaryland PLXOP21005-5066, PLXOYUnited States.
E-mail addresses: john.d.clayton1.civ@mail.mil, jdclayt1@umd.edu, johnclay@cims.nyu.edu (J.D. Clayton).

https://doi.org/10.1016/j.ijsolstr.2019.02.016
0020-7683/Published by Elsevier Ltd.

on internal state, leading to natural coupling among inelastic dilatation and shear, for example (Clayton, 2017b,c; Clayton and Knap, 2018a,b). This more advanced mathematical framework may be implemented for the present material systems in future studies. It is eschewed here in the interest of simplicity and computational efficiency, enabling isolated study of effects represented in traditional phase field theory (Clayton and Knap, 2016).

A geometrically linear theory is deemed sufficient for the small applied strains incurred at structural failure in simulations reported herein. A potential drawback of this simplification is that twinning shears are large; use of the geometrically linear approximation tends to result in similar homogenized model predictions for polycrystals as the geometrically nonlinear theory (Clayton and Knap, 2016), but in some cases it may produce differences in local twin morphologies (Clayton and Knap, 2011b).

Two heterogeneous ceramic materials are of interest in this work. The first is composed by majority of crystalline boron carbide (B_4C, rhombohedral structure), with secondary grains of crystalline titanium diboride (TiB_2, hexagonal structure). Grain sizes of each phase are comparable. Physical deformation and failure mechanisms and possible relationships to microstructure are discussed in Sigl and Kleebe (1995), White and Dickey (2011), and Demirskyi et al. (2017), for example. Single phase boron carbide polycrystals demonstrate favorably low mass density and extreme hardness, but they are brittle and may also undergo deformation twinning and a stress-induced crystal-to-glass transformation under severe compression and/or shear deformation (Chen et al., 2003; Clayton, 2012; An and Goddard, 2015; Clayton and Knap, 2018a). Recent experimental and computational modeling efforts aimed at engineering improved boron-based ceramics are described in Coleman et al. (2016). Titanium diboride, while heavier (i.e., higher mass density) and of lower hardness, may be more ductile than boron carbide as a result of dislocation activity (Vanderwalker and Croft, 1988). Secondary grains of the more ductile phase may improve overall fracture toughness and failure resistance by serving as obstacles to cleavage crack propagation through the boron carbide matrix. Intergranular fractures at phase boundaries may be forced to meander through the microstructure, further elevating overall toughness (Sigl and Kleebe, 1995). When processed by cooling from a higher temperature, compressive and tensile residual stresses may arise in B_4C and TiB_2, respectively, since thermal expansion coefficients are larger in the latter. These residual stresses may also improve failure resistance (White and Dickey, 2011).

The second ceramic composite studied herein is predominantly diamond (C, cubic structure) with secondary grains of silicon carbide (β-SiC, cubic structure). Physical deformation and failure mechanisms and possible relationships to microstructure are reported in Zhao et al. (2004), Yang et al. (2013), Liu et al. (2015), and Matthey et al. (2017). Diamond grains tend to be of equal or much larger size than SiC grains, and the latter may include layers of much smaller grains, perhaps even nano-structured, fully encapsulating the diamond. Silicon carbide is added to improved ductility and fracture toughness, since diamond alone, though the hardest and stiffest known of all natural solids, is brittle and prone to cleavage failure. Encasement of diamond in a SiC matrix may promote crack deflection and increase overall toughness. Stresses and/or temperatures must be very high to enable plastic deformation (e.g., dislocations, twins) in diamond (Field, 2012) and are not attained here. On the other hand, β-SiC may undergo deformation twinning which has been observed in experiments (Van Torne, 1966) and might be inferred from its very low intrinsic stacking fault energy (Ning and Ye, 1990). Stacking faults are profuse in the SiC phase of these composites (Matthey et al., 2017). Residual stresses may be incurred during thermal processing, with diamond in compression and SiC in tension after cooling to room temperature (Liu et al., 2015).

Polycrystalline materials consisting of multiple phases demonstrate complex mechanics at the nanoscale along their internal interfaces, where grains of multiple phases intersect. Gradients in chemical composition at phase boundaries may lead to corresponding variations in local properties such as stiffness and work of separation. Furthermore, tertiary phases comprising intergranular films may be present that further affect the mechanical response, as recognized in Reddy et al. (2012) for B_4C and Sigl and Kleebe (1995) for B_4C-TiB_2. In the diamond-SiC system, segregated amorphous carbon (Liu et al., 2014) or residual silicon (Matthey et al., 2017) may likewise affect the response.

Composition gradients along phase boundaries have been addressed by phase field models applied to problems involving interfaces in mechano-chemistry (Biswas et al., 2016; Verma et al., 2017). See also Clayton and Knap (2018b) where amorphous intergranular films are resolved explicitly in simulations of phase changes and fracture. A challenge of incorporation of such physics for fracture is proper selection of parameters like surface energy entering the total energy functional. Experimental measurements for such phase boundary properties are scarce if not nonexistent for materials of present interest, and parametric studies become unwieldy due to the large conceivable property space that should be probed. The present work treats interfaces between grains of different phases as perfectly bonded in their initial state, omitting tertiary boundary phases and composition gradients near interfaces. Results provide a baseline set of response data with which future studies incorporating special properties along phase boundaries can be compared.

Orientations of grains in polycrystalline solids also affect their local mechanical response. Bulk effects influencing stress fields include elastic and plastic anisotropy, while interfacial effects include the dependence of grain boundary energy and strength on lattice orientations. For example, tensile strength depending on misorientation in SiC bicrystals has been quantified using atomic simulations (Kohyama, 1999; Han and Tomar, 2016). Similar effects of orientation on strength are expected in B_4C, though they remain to be quantified (Coleman et al., 2016), and cleavage fracture is more prominent in this material (Sigl and Kleebe, 1995; Scharf and Rubink, 2018).

The present work accounts for bulk orientation effects through anisotropic fracture energy, i.e., cleavage planes, and through discrete planes and directions for slip, twinning, and potential phase changes. Effects of orientation on grain boundary properties are not included herein, but these have been addressed in other phase field approaches for multi-physics problems (Verma et al., 2017; Biswas et al., 2018). Similarly to the case of phase boundary property variations, parametric studies are currently hindered by the large property space and incomplete or nonexistent local experimental measurements. The current work again provides baseline results that can be compared with future data that should incorporate orientation-dependent grain boundary properties.

The remainder of this paper is organized as follows. A constitutive theory based on phase field mechanics is reported in §2. Equations are written in general forms encompassing physical behaviors possible in each specific material system of present interest. Application of the theory to B_4C-TiB_2 ceramics is reported in §3, wherein polycrystalline microstructures with various volume fractions of each phase, various initial lattice orientations, and various inelasticity mechanisms enabled are subjected to compressive loading. Application of analogous simulation protocols to polycrystalline diamond-SiC composites is reported in §4. Concluding remarks follow thereafter.

2. Phase field theory

The phase field theory used here is a generalization of the framework first reported in Clayton and Knap (2016), where, in addition to deformation twinning and fracture, other structural transformations such as solid-solid phase changes and accumulation and slip of partial and full dislocations and stacking faults are addressed. Regarding phase changes, an amorphization component of the theory (Clayton, 2014b) was implemented in FE simulations described in Clayton and Knap (2018a,b). The current presentation is restricted to geometrically linear kinematics and a quasi-static model of mechanical and phase equilibria.

2.1. Order parameters

Let $\boldsymbol{X}$ with Cartesian components X_K denote the reference position vector of a material particle. Two scalar order parameters are introduced. The first, denoted by $\xi \in [0, 1]$, is used to represent fracture, where

$$\begin{array}{l}\xi(\boldsymbol{X}) = 0 \forall \boldsymbol{X} \in \text{ undamaged material},\\ \xi(\boldsymbol{X}) \in (0, 1) \forall \boldsymbol{X} \in \text{partially degraded material},\\ \xi(\boldsymbol{X}) = 1 \forall \boldsymbol{X} \text{ fully failed material}.\end{array} \tag{2.1}$$

The second order parameter $\eta \in [0, 1]$ describes the following material states:

$$\begin{array}{l}\eta(\boldsymbol{X}) = 0 \forall \boldsymbol{X} \in \text{ parent elastic crystal},\\ \eta(\boldsymbol{X}) \in (0, 1) \forall \boldsymbol{X} \in \text{structural boundary zone},\\ \eta(\boldsymbol{X}) = 1 \forall \boldsymbol{X} \in \text{structurally transformed state}.\end{array} \tag{2.2}$$

Most generally, depending on the particular material, $\eta > 0$ is used to account for inelastic shearing from slip of full, partial, and/or twinning dislocations as well as localized slip in amorphous bands. It can also be used to account for densification (expansion) correlating with lower (higher) free volume in phase transformation zones. The set (η, ξ) will be referred to as the "internal state" of the material.

2.2. Kinematics

The displacement field is denoted by the vector $\boldsymbol{u} = \boldsymbol{u}(\boldsymbol{X})$. Let $\nabla(\cdot)$ denote the covariant derivative with respect to $\boldsymbol{X}$, which here reduces to a partial coordinate derivative in Cartesian coordinates. The displacement gradient is decomposed additively into elastic and state-dependent parts as in Clayton and Knap (2018a,b):

$$\nabla \boldsymbol{u}(\boldsymbol{X}) = \boldsymbol{\beta}^E(\boldsymbol{X}) + \boldsymbol{\beta}^D[\xi(\boldsymbol{X}), \eta(\boldsymbol{X})]. \tag{2.3}$$

The elastic distortion is written as $\boldsymbol{\beta}^E(\boldsymbol{X})$. If the internal state and total displacement gradient $\nabla \boldsymbol{u}$ are known, then $\boldsymbol{\beta}^E$ can be obtained from manipulation of (2.3). The state-dependent contribution evolves according to changes in microstructure (ξ, η). A sum of three terms for three possible physical mechanisms is used (Clayton and Knap, 2018a,b):

$$\boldsymbol{\beta}^D(\xi, \eta) = x_\xi \phi_\xi(\xi)\mathbf{1} + x_\eta \phi_\eta(\eta)\boldsymbol{M} \otimes \boldsymbol{M} + \gamma_0 \phi_0(\eta)\boldsymbol{S} \otimes \boldsymbol{M}. \tag{2.4}$$

The first term on the right side of (2.4) accounts for dilatation from cavitation or crack opening, the second for compression or extension normal to a material plane from phase changes, and the third for shearing from dislocation slip, twinning, or localized shear bands. For material systems of present interest, the same plane with unit normal vector $\boldsymbol{M}$ is attached to each of the latter two mechanisms. In other words, $\boldsymbol{M}$ is the plane upon which structural transformations, slip (i.e., the glide plane), twinning (i.e., the habit plane), and localized shear may occur. The direction of inelastic shearing is denoted by the unit vector $\boldsymbol{S}$. Though in principle numerous planes and directions are possible in real materials depending on mechanisms and structure, attention here is restricted to a single oriented system for each mechanism in a given crystal to keep 3D multi-million element calculations tractable. Otherwise, as explained in Clayton and Knap (2011a), distinct order parameters for each set of plane and direction would be necessary with a commensurate penalty in computational overhead.

The total strain tensor is denoted by $\boldsymbol{\epsilon}$ and the elastic strain by $\boldsymbol{\epsilon}^E$:

$$\boldsymbol{\epsilon} = \tfrac{1}{2}[\nabla \boldsymbol{u} + (\nabla \boldsymbol{u})^{\mathrm{T}}], \quad \boldsymbol{\epsilon}^E = \tfrac{1}{2}[\boldsymbol{\beta}^E + (\boldsymbol{\beta}^E)^{\mathrm{T}}]. \tag{2.5}$$

The function $\boldsymbol{\epsilon}^E = \boldsymbol{\epsilon}^E(\nabla \boldsymbol{u}, \xi, \eta)$ will enter the strain energy density. Each term in (2.4) is now defined precisely. Damage growth kinematics, via voids, cavitation, or crack opening, is idealized as isotropic (Clayton, 2014b; 2016), with the unit tensor $\mathbf{1}$ multiplied by the product of scalar x_ξ and the scalar function

$$\phi_\xi(\xi) = \alpha\xi^2 + 2(2 - \alpha)\xi^3 + (\alpha - 3)\xi^4. \tag{2.6}$$

Polynomial $\phi_\xi : [0, 1] \to [0, 1]$ is an interpolation function such that $\phi'_\xi(0) = \phi'_\xi(1) = 0$, and $\alpha \in [0, 6]$ is a constant (Levitas et al., 2009; Clayton and Knap, 2011a). Material constant x_ξ is positive for expansion. A change of solid phase coincides with uniaxial strain normal to the basal plane, for example as occurring in B_4C (Yan et al., 2009; Clayton, 2017c). Let interpolation be given by

$$\phi_\eta(\eta) = \beta\eta^2 + 2(2 - \beta)\eta^3 + (\beta - 3)\eta^4. \tag{2.7}$$

Polynomial $\phi_\eta : [0, 1] \to [0, 1]$ satisifies $\phi'_\eta(0) = \phi'_\eta(1) = 0$, and $\beta \in [0, 6]$ is a constant. Material constant x_η is negative for densification, positive for expansion. As in Clayton and Knap (2011a,b, 2013), twinning on a single system with unit habit plane normal $\boldsymbol{M}$ and orthogonal shearing direction $\boldsymbol{S}$ is an isochoric simple shear scaled in magnitude by the interpolation function

$$\phi_0(\eta) = \chi\eta^2 + 2(2 - \chi)\eta^3 + (\chi - 3)\eta^4, \tag{2.8}$$

with constant $\chi \in [0, 6]$. The maximum magnitude of twinning shear, to include possible shearing accommodated by localization in structural transformation zones, is γ_0. The same functions are used to account for slip of full or partial dislocations in direction $\boldsymbol{S}$ with slip plane normal $\boldsymbol{M}$, where γ_0 is a saturation limit for shear on a single glide system or family of systems (Clayton, 2017a; 2018).

The order parameters and kinematic description outlined above are sufficient to address inelastic mechanisms in ceramic composites reported later in §3 and §4. Generalizations may be necessary for other material systems.

2.3. Thermodynamics and general balance laws

The total energy functional for an initially heterogeneous body Ω with boundary $\partial\Omega$ is

$$\Psi(\boldsymbol{u}, \eta, \xi, \boldsymbol{X}) = \int_\Omega [W(\nabla \boldsymbol{u}, \eta, \xi, \boldsymbol{X}) + f(\eta, \xi, \nabla\eta, \nabla\xi, \boldsymbol{X})]\mathrm{d}V. \tag{2.9}$$

In a reference state, the body occupies volume V and is enclosed by surface S with unit outward normal vector $\boldsymbol{n}$. Initial material properties may vary with $\boldsymbol{X}$, for example in conjunction with orientations and phases of grains in a polycrystal. Position $\boldsymbol{X}$ is dropped from the explicit list of arguments in forthcoming derivations, whereby it is understood that properties are homogeneous within each sub-volume of material corresponding to a single crystal or grain boundary layer comprising a heterogeneous polycrystal. The same convention is implicitly followed in Clayton and Knap (2016, 2018a,b).

In the linear theory, strain energy per unit volume W is of the form

$$W = W[\boldsymbol{\epsilon}^E(\nabla \boldsymbol{u}, \eta, \xi), \eta, \xi] = \tfrac{1}{2}\boldsymbol{\epsilon}^E : \mathbf{C}(\eta, \xi, \nabla \cdot \boldsymbol{u}) : \boldsymbol{\epsilon}^E. \tag{2.10}$$

Here $\mathbf{C}$ denotes the fourth-order tensor of elastic moduli, which may most generally be anisotropic and depend on the order parameters. Function f accounts for internal state and order parameter gradients and is partitioned as Clayton and Knap (2016)

$$f(\eta,\xi,\nabla\eta,\nabla\xi)=f_0(\eta,\xi)+g_0(\xi)+f_1(\xi,\nabla\eta)+g_1(\nabla\xi). \tag{2.11}$$

Gradient-dependent terms in (2.11) further obey, with κ_0 and ω_0 material constants later related to surface energies in (2.22),

$$\begin{aligned} &f_1(\xi,\nabla\eta)=\boldsymbol{\kappa}(\xi):(\nabla\eta\otimes\nabla\eta),\quad \boldsymbol{\kappa}(\xi)=\kappa_0\hat{\imath}(\xi)\mathbf{1},\\ &g_1(\nabla\xi)=\boldsymbol{\omega}:(\nabla\xi\otimes\nabla\xi),\quad \boldsymbol{\omega}=\omega_0[\mathbf{1}+\hat{\beta}(\mathbf{1}-\boldsymbol{N}\otimes\boldsymbol{N})]. \end{aligned} \tag{2.12}$$

The coupling degradation function $\hat{\imath}:[0,1]\to[0,1]$ obeys $\hat{\imath}(0)=1$ and $\hat{\imath}(1)=\zeta$:

$$\hat{\imath}(\xi)=\zeta+(1-\zeta)(1-\xi)^2, \tag{2.13}$$

with ζ a scalar constant subject to $0<\zeta\ll 1$ that ensures a small residual energy and stiffness as $\xi\to 1$. Setting $\hat{\beta}\gg 1$ forces fractures to localize along cleavage planes oriented by unit normal vector $\boldsymbol{N}$. Conversely, $\hat{\beta}=0$ results in isotropic damage.

Stationary points of the total energy functional Ψ are obtained as solutions of the variational equation with $\boldsymbol{X}$ fixed:

$$\delta\Psi=\oint_{\partial\Omega}(\boldsymbol{t}\cdot\delta\boldsymbol{u}+r\delta\eta+s\delta\xi)\mathrm{d}S. \tag{2.14}$$

Assuming field variables are sufficiently smooth, local equilibrium equations (i.e., Euler-Lagrange equations at a local material point $\boldsymbol{X}$) and boundary conditions are then derived via application of the divergence theorem (Clayton and Knap, 2011a; 2016):

$$\nabla\cdot\left.\frac{\partial W}{\partial\nabla\boldsymbol{u}}\right|_{\eta,\xi}=\nabla\cdot\boldsymbol{P}=\mathbf{0}; \tag{2.15}$$

$$\begin{aligned} &\frac{\partial f}{\partial\eta}-2\nabla\cdot(\boldsymbol{\kappa}\nabla\eta)+\left.\frac{\partial W}{\partial\eta}\right|_{\nabla\boldsymbol{u},\xi}=0,\\ &\frac{\partial f}{\partial\xi}-2\nabla\cdot(\boldsymbol{\omega}\nabla\xi)+\left.\frac{\partial W}{\partial\xi}\right|_{\nabla\boldsymbol{u},\eta}=0; \end{aligned} \tag{2.16}$$

$$\boldsymbol{t}=\boldsymbol{P}\cdot\boldsymbol{n},\quad r=2\boldsymbol{\kappa}:(\nabla\eta\otimes\boldsymbol{n}),\quad s=2\boldsymbol{\omega}:(\nabla\xi\otimes\boldsymbol{n}). \tag{2.17}$$

The stress tensor $\boldsymbol{P}$ is always symmetric in the geometrically linear theory. The mechanical traction vector is $\boldsymbol{t}$; the conjugate surface force to the order parameter η is r; the conjugate surface force to the order parameter ξ is s. The governing equations listed above apply for the general framework of (2.9), with (2.15) and (2.16) applicable within volume Ω and (2.17) the natural boundary conditions on its boundary $S=\partial\Omega$.

2.4. Energy density, reduced governing equations, and numerical methods

Isotropic linear elasticity is used hereafter for simplicity and computational efficiency, where the strain energy density per unit volume is

$$W=\tfrac{1}{2}\lambda(\mathrm{tr}\boldsymbol{\epsilon}^E)^2+\mu\boldsymbol{\epsilon}^E:\boldsymbol{\epsilon}^E. \tag{2.18}$$

Lamé coefficients μ and λ depend on ξ and possibly elastic volume change:

$$\begin{aligned} &\mu(\xi)=\mu_0[\zeta+(1-\zeta)(1-\xi)^2],\\ &\lambda(\xi,\mathrm{tr}\boldsymbol{\epsilon}^E)=k(\xi,\mathrm{tr}\boldsymbol{\epsilon}^E)-\tfrac{2}{3}\mu(\xi); \end{aligned} \tag{2.19}$$

$$k(\xi,\mathrm{tr}\boldsymbol{\epsilon}^E)=(\lambda_0+\tfrac{2}{3}\mu_0)\{[\zeta+(1-\zeta)(1-\xi)^2]\langle\mathrm{tr}\boldsymbol{\epsilon}^E\rangle+\langle-\mathrm{tr}\boldsymbol{\epsilon}^E\rangle^*\}, \tag{2.20}$$

where the operator $\langle x\rangle=1\forall x>0$, $\langle x\rangle=0\forall x\le 0$, $\langle x\rangle^*=1\forall x\ge 0$, and $\langle x\rangle^*=0\forall x<0$ Clayton and Knap (2014). Accordingly, bulk modulus k degrades with fracture under tensile pressure but not under compressive pressure, such that behavior is fluid-like for $\xi\to 0$. Shear modulus μ can degrade in tension and compression.

Potential energy functions that depend on order parameters but not their gradients in (2.11) are defined as follows, where H(·) is the Heaviside step function (Clayton and Knap, 2018a):

$$f_0(\eta,\xi)=[A\eta^2(\eta_0-\eta)^2\mathrm{H}(\eta_0-\eta)+\hat{A}\eta^2]\hat{\imath}(\xi),\quad g_0(\xi)=B\xi^2. \tag{2.21}$$

The first term in square braces in f_0 is a double-well potential with minima at $\eta=(0,\eta_0)$, a local maximum at $\eta=\eta_0/2$, and a cut-off demarcated by $\eta_0>0$. Quadratic forms are given by the remaining term in f_0 and the entire function g_0, where the latter is standard in phase field modeling of fracture (Borden et al., 2012; Clayton and Knap, 2014).

Material constants in (2.21) are A, η_0, $\hat{A}$, and B. Let Γ denote the twin boundary energy or intrinsic stacking fault energy associated with twinning or partial dislocations. Let Υ denote the fracture surface energy. Denote two regularization lengths by l_η and l_ξ. Consulting (2.12) and (2.21), material constants entering the phase energy potentials are related by extension of deriviations in Clayton and Knap (2011a, 2016):

$$A=12\frac{\Gamma}{\eta_0^4 l_\eta},\quad \kappa_0=\frac{3}{4}\frac{\Gamma l_\eta}{\eta_0^2};\quad B=\frac{\Upsilon}{l_\xi},\quad \omega_0=\Upsilon l_\xi. \tag{2.22}$$

Constant $\hat{A}$ is an energy barrier for phase changes (Clayton and Knap, 2018a) and can also account for stored energy of dislocation lines (Clayton, 2018). More precise relations to physical characteristics of particular crystal types follows later in §3 and §4.

Reduced governing equations are obtained by differentiation of the functions in (2.11), (2.12), (2.18), and (2.21) and insertion of the results into (2.15) and (2.16). The derivatives below enter these Euler-Lagrange equations:

$$\boldsymbol{P}=\left.\frac{\partial W}{\partial\nabla\boldsymbol{u}}\right|_{\eta,\xi}=\lambda(\mathrm{tr}\boldsymbol{\epsilon}^E)\mathbf{1}+2\mu\boldsymbol{\epsilon}^E+\tfrac{1}{2}\lambda(\mathrm{tr}\boldsymbol{\epsilon}^E)^2\frac{\partial k}{\partial(\mathrm{tr}\boldsymbol{\epsilon}^E)}\mathbf{1}, \tag{2.23}$$

$$\begin{aligned} \frac{\partial f}{\partial\eta}=&\left\{2\hat{A}\eta+\frac{\mathrm{d}}{\mathrm{d}\eta}[A\eta^2(\eta_0-\eta)^2\mathrm{H}(\eta_0-\eta)]\right\}\\ &\times[\zeta+(1-\zeta)(1-\xi)^2], \end{aligned} \tag{2.24}$$

$$\frac{\partial f}{\partial\nabla\eta}=2\boldsymbol{\kappa}\nabla\eta,\quad \frac{\partial f}{\partial\nabla\xi}=2\boldsymbol{\omega}\nabla\xi, \tag{2.25}$$

$$\begin{aligned} \frac{\partial f}{\partial\xi}=&2B\xi-2[(1-\zeta)(1-\xi)][\kappa_0|\nabla\eta|^2\\ &+A\eta^2(\eta_0-\eta)^2\mathrm{H}(\eta_0-\eta)+\hat{A}\eta^2], \end{aligned} \tag{2.26}$$

$$\left.\frac{\partial W}{\partial\xi}\right|_{\nabla\boldsymbol{u},\eta}=\varsigma=\tfrac{1}{2}\left(\frac{\partial k}{\partial\xi}-\tfrac{2}{3}\frac{\partial\mu}{\partial\xi}\right)(\mathrm{tr}\boldsymbol{\epsilon}^E)^2+\frac{\partial\mu}{\partial\xi}\boldsymbol{\epsilon}^E:\boldsymbol{\epsilon}^E, \tag{2.27}$$

$$\begin{aligned} &\frac{\partial k}{\partial\xi}=-2(\lambda_0+\tfrac{2}{3}\mu_0)\{[(1-\zeta)(1-\xi)]\langle\mathrm{tr}\boldsymbol{\epsilon}^E\rangle\},\\ &\frac{\partial\mu}{\partial\xi}=-2\mu_0(1-\zeta)(1-\xi). \end{aligned} \tag{2.28}$$

Derivative $(\partial W/\partial\eta)|_{\nabla\boldsymbol{u},\xi}$ providing the elastic driving force for slip, twinning, or phase changes can be obtained analytically (see, e.g., Clayton and Knap, 2016; Clayton and Knap, 2018a for relevant terms) but is too lengthy to list here in entirety.

Table 1
Physical properties or model parameters for B_4C and TiB_2.

Parameter [units]	Definition	Value - B_4C	Value - TiB_2
μ_0 [GPa]	initial shear modulus	193	249
λ_0 [GPa]	initial Lamé modulus	108	27
c, a [nm]	lattice parameters	1.21, 0.56	0.323, 0.303
Υ [J/m^2]	fracture energy	3.27	4.14
Γ [J/m^2]	twin boundary or SF energy	0.54	3.6 (0.12)
$\hat{\beta}$	fracture anisotropy	100	100
l [μm]	regularization length	0.1	0.1
γ_0	max twin shear or plastic slip	0.31	0.015
η_0	cut-off for double-well energy	0.68	0.68
$\hat{A}$ [MPa]	phase or dislocation energy	188	11.4
x_η, x_ξ	phase densification, cavitation	–0.04, 0	0, 0
α, β, χ	kinematic interpolation	–, 0, 6	–, –, 6

General 3D boundary value problems are solved incrementally using the FE method. The procedure implemented here is similar to that of Clayton and Knap (2011a, 2016, 2018a), extended to account for the more general constitutive behavior outlined above in §2. Boundary conditions for displacement and order parameters, or their conjugate forces, are updated during each load increment. Numerical algorithms apply conjugate gradient energy minimization.

Candidate fields $\boldsymbol{u}(\boldsymbol{X})$, $\eta(\boldsymbol{X})$, $\xi(\boldsymbol{X})$ are obtained that minimize Ψ subject to boundary constraints and thereby satisfy (2.14). Multiple minima may exist, and non-unique and meta-stable solutions may be obtained since Ψ is generally non-convex. In forthcoming simulations, loading proceeds into the globally strain-softening regime, wherein incremental solutions are obtained after the first of either a minimum residual force tolerance or a maximum number of iterations is reached. Accuracy may be unavoidably compromised for the latter condition, a limitation that should be recalled when interpreting numerical results. When global tangent stiffness is positive in the appropriate sense, the former more strict force tolerance ensuring static equilibrium is always attained.

To enforce irreversibility of crack extension, constraints such as $\delta\xi(\boldsymbol{X}) \geq 0$ for $\xi(\boldsymbol{X})$ exceeding some threshold value ξ_T are imposed. Similarly, constraints such as $\delta\eta(\boldsymbol{X}) \geq 0$ for $\eta(\boldsymbol{X})$ exceeding a threshold value η_T are imposed to render twinning, slip, and/or phase changes irreversible. Accordingly, the incremental energy minimization problem translates to minimization of the energy of an alternative system with certain increment-dependent free boundaries along which $\xi \geq \xi_T$ is prescribed. An analogous interpretation of evolving internal boundary conditions for irreversible structure changes applies for $\eta \geq \eta_T$. Local Euler-Lagrange equations are satisfied by numerical solutions acquired for this alternative system.

3. Boron carbide-titanium diboride composites

Modeling of boron carbide-titanium diboride (B_4C-TiB_2) is reported next. Specialization of the general theory of §2 to each kind of crystal comprising the ceramic is discussed first, with associated physical properties entering each description. Finite element renderings of polycrystals with boundary conditions are discussed, and results of simulations are analyzed subsequently.

3.1. Constitutive models and material properties

Properties for each crystal type are listed in Table 1. The constitutive model for B_4C crystals corresponds to that presented in Clayton and Knap (2018a,b), with the exception that dependence of the metric tensor on internal state, i.e., the Finsler component of that theory, is omitted here for simplicity. Twinning occurs on $\langle 10\bar{1}0\rangle\{0001\}$ (An et al., 2014; An and Goddard, 2015; Li et al., 2010), yielding $\boldsymbol{S}$ and $\boldsymbol{M}$, fracture on basal {0001} planes, yielding $\boldsymbol{N}$. Amorphous shear bands can form within twinned domains (An et al., 2014; An and Goddard, 2015). Twinning shear is $\gamma_0 = \frac{2}{3}$a/c. The surface energy resisting twin formation is $\Gamma = \tau b = \frac{1}{3}\tau$a with b the magnitude of Burgers vector of twinning partial dislocations and $\tau = 2.9$ GPa the resolved shear stress for twinning.

The minimum regularization length is the process zone size (Rice, 1968; Clayton et al., 2012; Clayton, 2017b), $l_\xi \approx 1$ nm. This length is also physically appropriate for regularization of twin and phase boundaries (Grady, 2011), such that $l_\eta = l_\xi \to l$. This minimum value of l is satisfactory for simulations of nanocrystals (Clayton and Knap, 2018a) whose grain sizes are on the order of tens of nm. In simulations of polycrystals with conventional grain sizes, l is increased beyond its minimum proportionally to the grain size (Clayton and Knap, 2015; 2018b), here by a factor of 100 leading to the value in Table 1. Initiation of twinning kinematics precedes amorphous densification (Clayton and Knap, 2018a), justifying $\eta_0 < 1$ and parameters β and χ, all consistently with (2.1), (2.2), (2.7), and (2.8). A 4% volume reduction (Yan et al., 2009) from lattice collapse normal to (0001) along $\boldsymbol{M}$ produces x_η. Cavitation is omitted for compression problems studied herein, so x_ξ vanishes, rendering α of (2.6) superfluous. Energy barrier $\hat{A}$ is obtained from (Fanchini et al., 2006), fracture surface energy Υ from (Beaudet et al., 2015), cleavage anisotropy $\hat{\beta}$ from (Clayton and Knap, 2015), elastic constants μ_0 and λ_0 from Clayton (2012).

The phase field constitutive model for TiB_2 is newly introduced here, with properties given in the rightmost column of Table 1. Elastic constants are reported from (Dandekar and Benfanti, 1993; Clayton, 2014a). Values of l, η_0, $\hat{\beta}$, and χ are chosen realistically and consistently with those for B_4C. The plane of minimum fracture energy is the basal plane, such that cleavage occurs on {0001}, giving $\boldsymbol{N}$, with Υ obtained from DFT calculations of Du and Chen (2018). In (2.21), η is used to account for stacking fault energy from partial dislocation slip via A and for stored line energy of dislocations via $\hat{A}$. It also is used to interpolate from null to maximum plastic slip γ_0 on a single glide system in (2.4) and (2.8). Inelastic volume changes are not considered substantial, leading to null x_η and x_ξ.

Physically, η can be related to a combination of the magnitude of the Burgers vector of a partial dislocation b as well as the cumulative dislocation density ρ_D. The glide system with lowest stacking fault (SF) energy barrier $\Gamma = 3.6$ J/m^2 for hexagonal TiB_2 according to DFT calculations (Du and Chen, 2018) corresponds to basal slip $\langle 11\bar{2}0\rangle\{0001\}$ with the full Burgers vector $b_0 = $ a. Since very limited plastic deformation is observed in this ceramic at room temperature, single slip conditions are enforced, with $\boldsymbol{S}$ and $\boldsymbol{M}$ prescribed accordingly for one of three possible systems on the basal plane. Additional calculations are undertaken with a smaller value of $\Gamma = 0.12$ J/m^2 for the stacking fault energy of TiB_2 as inferred from separation distances of partial dislocations (Vanderwalker and Croft, 1988).

Let $\bar{x}$ denote the maximum distance a (partial) dislocation travels prior to arrest, with a value of $\bar{x} = 50$ nm inferred from observations in Vanderwalker and Croft (1988). Let ρ_S denote the saturation density of dislocations, reasonably $\rho_S = 10^{15}$m^{-2}. Stored energy density from dislocation lines is $\frac{1}{2}\mu_0 b^2 \rho_D$ (Clayton, 2011b; 2018). Then for the phase field model for partial slip in TiB_2,

$$\eta = (b/b_0)\sqrt{\rho_D/\rho_S}, \quad \gamma_0 = \rho_S b_0 \bar{x}, \quad \hat{A} = \tfrac{1}{2}\mu_0 b_0^2 \rho_S. \tag{3.1}$$

With (3.1) depending on fundamental physics, no parameters need be artificially calibrated to obtain numerical results.

Residual stresses induced during thermal processing of B_4C-TiB_2 composites may be important for overall fracture toughness (Scharf and Rubink, 2018). These are omitted here and will be addressed in future work. Initial porosity, inclusions, and layers of tertiary phases are also postponed for later studies. Prior research

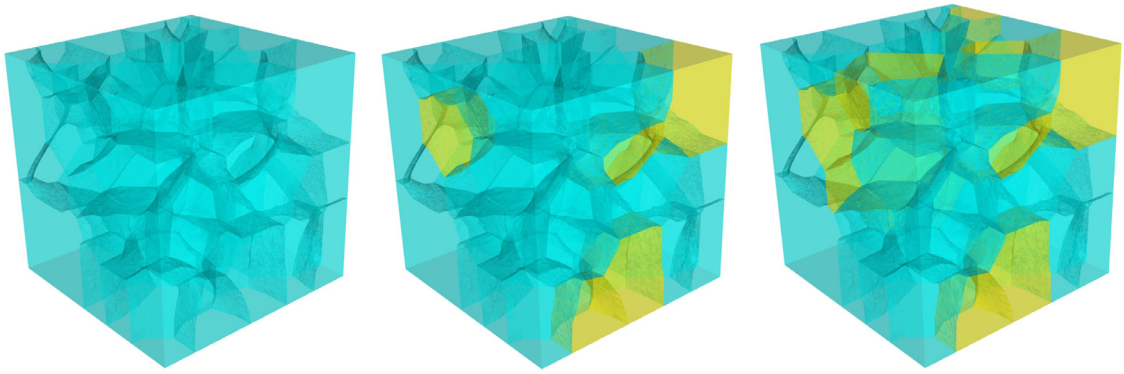


Fig. 1. Meshes for B_4C-TiB_2; (B_4C, TiB_2) crystals are (teal, yellow) and V_2 is the volume fraction of TiB_2: (a) microstructure 1, $V_2 = 0$ (b) microstructure 2, $V_2 = 0.10$ (c) microstructure 3, $V_2 = 0.18$.

has suggested that intergranular layers of amorphous carbon or boron nitride may improve fracture resistance (Reddy et al., 2012; Clayton and Knap, 2018b).

3.2. Microstructure rendering and boundary conditions

A polycrystalline aggregate of 50 polyhedral-shaped crystals is rendered. The methodology for generating this and similar FE meshes is reported in Clayton et al. (2012). The edge length of the cube-shaped polycrystalline domain Ω is $L = 10\,\mu$m, and the average grain size is $L/50^{1/3} \approx 2.5\,\mu$m. Let phases 1 and 2 correspond to B_4C and TiB_2, respectively. Three microstructure morphologies are considered, each with different volume fractions V_2 of phase 2 ranging from 0 to 18%, as shown in Fig. 1. These ranges are within those of real composite materials that have been fabricated and characterized (Scharf and Rubink, 2018). Microstructures 2 and 3 contain five and ten randomly distributed TiB_2 crystals, respectively. For each microstructure, two different distributions of random lattice orientations associated with (***S, M, N***) are assigned to the grains. Finally, for each of these six cases (i.e., three microstructures $\times$ two orientation sets), one simulation is performed with structural transformations of twinning, amorphization, and plastic slip enabled using the properties quoted in Table 1, and a second simulation is performed with these transformations suppressed, i.e., $\eta(\boldsymbol{X}) = 0 \forall \boldsymbol{X} \in \Omega$ is enforced. Two simulations for each of microstructures 2 and 3 are also performed, with transformations enabled, using a smaller value of $\Gamma = 0.12$ J/m^2. The total number of simulations reported in §3 is thus sixteen. Fracture, via $\xi(\boldsymbol{X}) > 0$, is possible in all.

Displacement boundary conditions on $\partial\Omega$ leading to uniaxial compressive stress are applied. One face of the aggregate is held fixed in the loading direction, with displacement applied uniformly to the opposite face. The aggregate is constrained to eliminate rigid body modes. Lateral surfaces are free to expand to maintain an overall 1D stress state, meaning traction $\boldsymbol{t}$ of (2.17) vanishes on lateral faces. Regarding order parameters, free boundary conditions $r = s = 0$ are assigned on all six faces of the cube comprising $\partial\Omega$. Irreversibility is ensured by setting $\xi_T = \eta_T = 0.9$ (Clayton and Knap, 2016).

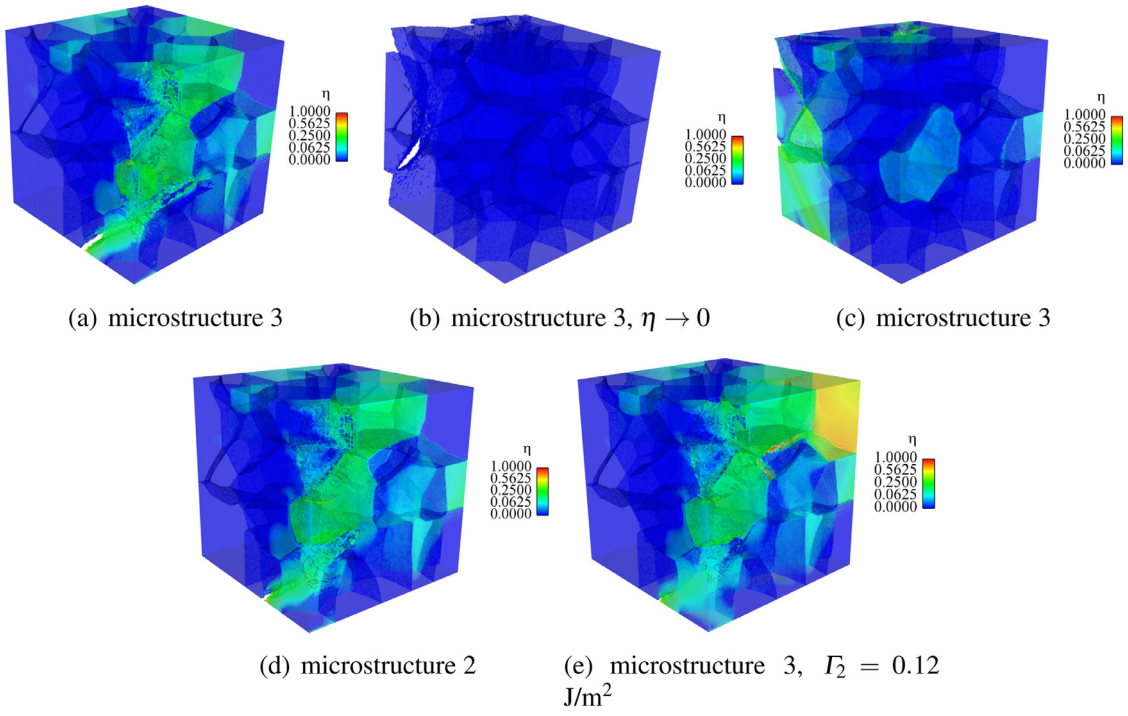
3.3. Finite element simulations and analysis of results

Results of the FE simulations for B_4C-TiB_2 are summarized next. Representative contours of η, denoting twinning, shear localization, and amorphization in B_4C crystals and basal slip in TiB_2 crystals are shown in Fig. 2. Scale bars are quadratic to enable visualization of low levels of transformation ($0 \lesssim \eta \lesssim 0.25$), which occur primarily in B_4C crystals, physically representative of partial structural transformations. Slip in TiB_2 crystals, which can be identified via reference to Fig. 1, is nearly negligible for all cases except that shown in Fig. 2(e), the only result shown that invokes the smaller value of $\Gamma = \Gamma_2$ for the TiB_2 phase. In this particular case, dislocation slip is more prominent in phase 2, especially in the grain located in the upper right corner of the aggregate.

Fracture and transformation behaviors appear very similar for microstructures 2 and 3 in Fig. 2(d) and (a), as these behaviors occur predominantly in the weaker B_4C grains. Transformations ($\eta > 0$) are prohibited in the case shown in Fig. 2(b), which demonstrates a different fracture path than Fig. 2(d) and (a), traversing B_4C grains and following phase boundaries between B_4C and TiB_2. The case shown in Fig. 2(c) invokes a different set of lattice orientations than the other cases in Fig. 2. Notably different crystals undergo transformation ($\eta > 0$), and the fracture behavior is similar to that when transformations are suppressed in Fig. 2(b).

Volume-averaged axial compressive stress and order parameters are labeled $\bar{P}$, $\bar{\eta}$, and $\bar{\xi}$, respectively. These are reported versus applied axial compressive nominal strain $\bar{\epsilon}$ in Fig. 3. Average stresses for simulations featuring lattice orientation sets 1 and 2 are shown in respective Fig. 3(a) and (b). Stiffer responses are obtained with structural transformations suppressed via $\eta = 0$. Physically, more compliance results from deformation accommodation from transformations $\eta > 0$, with slip, twinning, and/or shear bands accommodating deviatoric deformation and, for B_4C grains, amorphous densification accommodating compressive volumetric deformation normal to planes of inelastic shear. Trends in average results are similar for orientation sets 1 and 2, with minor differences evident only upon close comparison of like-labeled curves in Fig. 3(a) and (b). Maximum compressive stress $P_C = \max_{\bar{\epsilon}}(\bar{P})$ decreases with increasing transformation activity. Ductility ϵ_C, defined as the applied strain $\bar{\epsilon}$ corresponding to peak load P_C, is likewise compromised by inelasticity associated with $\eta > 0$. All curves in Figs. 3 and 4, when transformations are enabled, invoke the larger value of Γ_2 from Table 2.

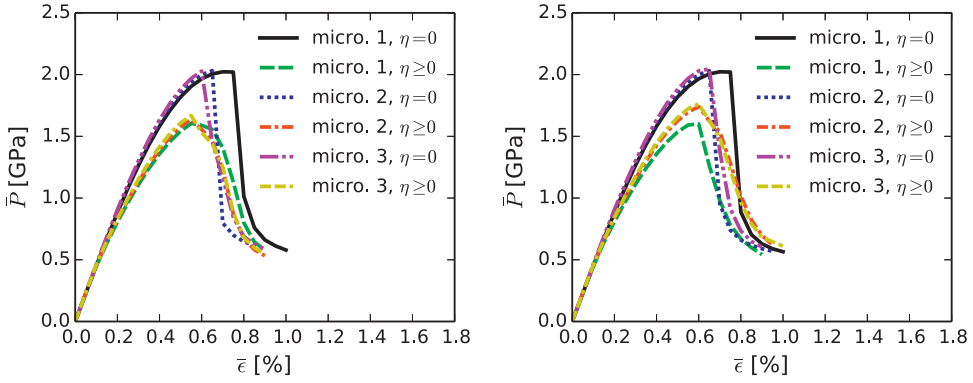
Average fracture order parameter $\bar{\xi}$ for orientation set 1 is shown in Fig. 4(a). Results are similar for orientation set 2, not shown. Similar observations, i.e., average stress-strain and fracture behaviors relatively insensitive to orientation, were noted for different ceramic microstructures and boundary conditions in Clayton and Knap (2018a,b). Microstructure 1 with $\eta = 0$ demonstrates the largest values of $\bar{\xi}$, though it is also one of the stiffest cases in Fig. 3. This suggests that the average damage parameter is not an accurate measure of overall strength degradation, which is instead associated with the formation of one or a few dominant cracks that may not be reflected in $\bar{\xi}$. Similar conclusions were drawn in



(a) microstructure 3 (b) microstructure 3, $\eta \to 0$ (c) microstructure 3

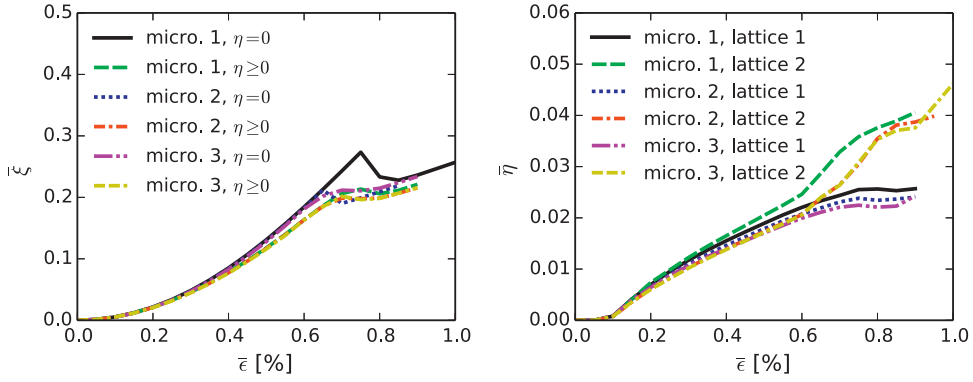
(d) microstructure 2 (e) microstructure 3, $\Gamma_2 = 0.12$ J/m^2

Fig. 2. Order parameter η for B_4C-TiB_2 at applied compressive strain $\bar{\epsilon} = 0.7\%$ with highly degraded elements ($\xi > 0.8$) visually removed to show fractures: (a) $V_2 = 0.18$, lattice 2 (b) $V_2 = 0.18$, lattice 2, no slip/twinning (c) $V_2 = 0.18$, lattice 1 (d) $V_2 = 0.10$, lattice 2 (e) $V_2 = 0.18$, lattice 2, easier slip in phase 2.



(a) lattice orientation set 1 (b) lattice orientation set 2

Fig. 3. Average axial stress $\bar{P}$ versus applied compressive strain $\bar{\epsilon}$ for B_4C-TiB_2.



(a) lattice orientation set 1 (b) both orientation sets

Fig. 4. Average order parameters versus applied compressive strain $\bar{\epsilon}$ for B_4C-TiB_2 for (a) fracture $\bar{\xi}$ (b) twinning, phase changes, and slip $\bar{\eta}$.

Table 2
Peak compressive stress (P_C), associated strain (ϵ_C), and averaged order parameters ($\bar{\xi}_C, \bar{\eta}_C$) for B_4C-TiB_2 composites.

Microstructure (fraction TiB_2)	Lattice orientation	Slip/twins active	P_C [GPa]	ϵ_C [%]	$\bar{\xi}_C$	$\bar{\eta}_C$
1 ($V_2 = 0$)	1	N	2.02	0.70	0.24	–
	1	Y	1.60	0.55	0.14	0.021
	2	N	2.02	0.70	0.24	–
	2	Y	1.60	0.60	0.16	0.025
2 ($V_2 = 0.10$)	1	N	2.03	0.65	0.21	–
	1	Y	1.64	0.55	0.14	0.019
	2	N	2.03	0.65	0.21	–
	2	Y	1.74	0.60	0.17	0.021
($\Gamma_2 = 0.12$ J/m^2)	1	Y	1.63	0.55	0.14	0.024
	2	Y	1.70	0.60	0.16	0.038
3 ($V_2 = 0.18$)	1	N	2.03	0.60	0.18	–
	1	Y	1.67	0.55	0.14	0.019
	2	N	2.05	0.70	0.22	–
	2	Y	1.76	0.60	0.16	0.021
($\Gamma_2 = 0.12$ J/m^2)	1	Y	1.66	0.55	0.14	0.027
	2	Y	1.68	0.55	0.14	0.036

Clayton and Knap (2018a). Evolution of $\bar{\xi}$ is not drastically different among the other cases shown in Fig. 4(a).

Average structure change parameter $\bar{\eta}$ for six simulations wherein transformations are enabled is shown in Fig. 4(b). Lattice orientation set 2 demonstrates more transformation activity than lattice orientation set 1 as measured by $\bar{\eta}$. Microstructure 1, consisting of pure B_4C, shows more structure change associated with $\bar{\eta}$ than microstructures 2 and 3 that contain increasing volume fractions of TiB_2. This observation is consistent with contours of Fig. 2 that indicate little or no slip activity in the TiB_2 phase, with the exception of Fig. 2(e) that invokes the lower value of stacking fault energy. For the present model and loading conditions, it is evident that fracture, and to a lesser extent twinning and phase changes, occur predominantly in B_4C, resulting in overall failure of the aggregate before driving forces sufficient for slip or fracture are attained in the stronger TiB_2 grains. Resistance to fracture and other structure changes in the two ceramic crystal types can be inferred from values of Υ and Γ, respectively, in Table 1, both of which are nominally larger for TiB_2.

Average data are presented for quantitative comparison of peak stress, ductility/strain, and order parameters in Table 2. Unconfined compressive strength P_C is around 2 GPa for cases with slip and twinning deactivated and around 1.7 GPa for cases with $\eta > 0$ enabled. These values are within ranges of static unconfined compressive strength measured for pure commercial B_4C with comparable grain sizes (grain diameters on the order of a few microns), providing some validation of the present results. Specifically, experimental ranges of $1 \lesssim P_C \lesssim 3$ GPa are reported in Reddy et al. (2012) and references therein, with a micro-pillar of comparable dimensions and grain sizes to the aggregates simulated here demonstrating a peak strength of just over 2 GPa. Comparison with experimental peak stress data are insufficient, however, to resolve whether structural changes such as slip, shear banding, and amorphization are active in micro-crystalline B_4C-TiB_2 under static uniaxial compressive loading. If so, the present simulations suggests that such activity occurs only on a very limited basis as indicated by the low values of $\bar{\eta}$ and η_C. Atomic and continuum models as well as experiments indicate that deformation twinning and amorphization are more prevalent in small samples of material deformed intensely to large strains, e.g., in small regions directly under indentation or impact. However, no amorphization was detected in compression of micro-pillars in Reddy et al. (2012), though it was found in nano-indentation.

Calculations—two simulations for each of microstructures 2 and 3—using a smaller value of $\Gamma_2 = 0.12$ J/m^2 for the stacking fault energy of TiB_2 (Vanderwalker and Croft, 1988) resulted in minor slip activity in preferentially oriented crystals, a slight reduction in peak axial stress, and no improvement in overall ductility relative to cases presented in figures herein obtained using the nominal larger value of $\Gamma = 3.6$ J/m^2 from Table 1 (Du and Chen, 2018). Corresponding results are listed for comparison in Table 2. Contours demonstrating increased slip are evident in Fig. 2(e). Dislocations have been observed in the titanium diboride grains in B_4C-TiB_2 (Scharf and Rubink, 2018), but their mobility and commensurate contribution to strain are unclear.

Peak stress P_C changes very little with increasing V_2 when slip/twinning and phase changes are disabled, i.e., addition of TiB_2 to B_4C does not appear to increase overall compressive strength of the composite when modeled as an elastic-perfectly brittle solid. Ductility is reduced with increasing V_2 in these cases, as is evident from Fig. 3. In contrast, when inelastic deformation mechanisms are enabled via $\eta > 0$, then the presence of TiB_2 in microstructures 2 and 3 provides a slight increase in P_C relative to microstructure 1, with ductility uncompromised.

Values of ϵ_C, $\bar{\xi}_C$, and $\bar{\eta}_C$ listed in Table 2 confirm trends mentioned already. Ductility decreases slightly with increasing transformation activity and with increasing TiB_2 content. Distributed damage as measured by $\bar{\xi}_C$ also decreases significantly when slip/twins are enabled and decreases slightly with increasing V_2.

Preliminary test data (Scharf and Rubink, 2018) show that fracture toughness of polycrystalline B_4C may be improved by 10–100% and flexure strength by 10–30% via addition of 13–23% TiB_2. The present results, on the other hand, demonstrate only modest improvements with increases in the TiB_2 fraction. Residual stresses induced by TiB_2 during thermal processing are thought to be substantial and compressive in the B_4C phase (White and Dickey, 2011; Demirskyi et al., 2017), which would tend to inhibit fracture but promote densification. It is possible that these initial residual stresses provide an overall strengthening effect, since the present results without residual stresses show that B_4C is the weaker phase wherein cleavage cracks concentrate. Furthermore, phase boundaries and GBs may increase toughness by deflecting cleavage cracks in the more brittle B_4C phase. Preferred intergranular fracture is observed between phases in some simulations, e.g., Fig. 2(b) that showed the largest average compressive strength, $P_C = 2.05$ GPa. The domain size studied in the present simulations may be too small to address blunting of longer cracks by the TiB_2 phase that could positively affect macroscopic fracture toughness in the composite.

Future work should consider incorporating residual stresses and distinct grain and phase boundary properties (with composition and orientation dependence) in simulations of many more mi-

Table 3
Physical properties or model parameters for diamond (C) and β-SiC.

Parameter [units]	Definition	Value – C	Value – SiC
μ_0 [GPa]	initial shear modulus	553	203
λ_0 [GPa]	initial Lamé modulus	73	90
a [nm]	lattice parameter	0.357	0.436
Υ [J/m^2]	fracture energy	5.30	1.70
Γ [J/m^2]	twin boundary or SF energy	–	0.034
$\hat{\beta}$	fracture anisotropy	100	100
l [μm]	regularization length	0.1	0.1
γ_0	max twin shear or plastic slip	–	0.707

crostructures, including larger domains with more grains of numerous orientation distributions. Demonstrations of the latter are shown later for a different ceramic at the conclusion of §4. Also of possible importance are elastic anisotropy, elastic nonlinearity, tertiary phases (e.g., inclusions and impurities), initial porosity, and activation of multiple slip, twin, and cleavage systems per crystal. Simultaneous consideration of all potential physical mechanisms is presently prohibited by computational cost. With regard to material design, the present results, with stated limitations, imply that strength should be improved by efforts that inhibit cleavage fracture and/or suppress shear localization of the B_4C phase, including addition of TiB_2.

4. Diamond-silicon carbide composites

Modeling of diamond-silicon carbide (C-SiC) is reported in the present section. Specialization of the general theory of §2 to each kind of crystal in the composite is presented first in conjunction with associated physical properties entering each description. Finite element renderings of microstructures are discussed. Results of simulations follow thereafter.

4.1. Constitutive models and material properties

Properties for each crystal type are listed in Table 3. As remarked in §1, diamond is modeled as an elastic-brittle material since plastic slip, twinning, and other structural transformations are not relevant for loading conditions of present interest. Therefore, parameters Γ, η_0, γ_0, x_η, $\hat{A}$, β, and χ are not needed for diamond. Cavitation is also excluded for compressive loading, such that $x_\xi = 0$ and α is not used. Elastic constants and fracture surface energy are obtained from (Field, 2012), where the latter corresponds to cleavage on {111} planes (i.e., those of the lowest surface energy), yielding vector $\boldsymbol{N}$. As in §3, a single dominant cleavage plane is prescribed for each crystal in forthcoming simulations, where anisotropy follows from the value of $\hat{\beta}$ listed in Table 3. Likewise, the same value of regularization length $l_\xi = l$ used for the hard ceramic B_4C is also used here for diamond.

Silicon carbide is modeled as an elastic solid that may undergo fracture and deformation twinning, respectively monitored by order parameters ξ and η. Elastic constants are obtained from (Erhart and Albe, 2005), with μ_0 the Voigt shear modulus computed from anisotropic single crystal constants. Planes of lowest surface energy for fracture are {110}, giving $\boldsymbol{N}$, with the value of Υ obtained from (Kikuchi et al., 2005). A single dominant cleavage plane and single dominant twinning system are assumed, consistent with the model of B_4C presented in §3 and Clayton and Knap (2018a,b). Twinning in the zinc blende strucure occurs on $\langle 11\bar{2}\rangle\{111\}$, giving $\boldsymbol{S}$ and $\boldsymbol{M}$, with a magnitude of $\gamma_0 = \sqrt{2}/2$ (Van Torne, 1966; Christian and Mahajan, 1995; Clayton, 2011b). The intrinsic stacking fault energy Γ linked to the process, obtained from Ning and Ye (1990), is notably low for a ceramic. Phase changes and inelastic volumetric deformation are not relevant for β-SiC under the forthcoming loading conditions, so x_ξ, x_η, α, β, and $\hat{A}$ are not needed. Remaining parameters $l_\xi = l_\eta = l$, η_0, $\hat{\beta}$, and χ are viewed as universal among the ceramics of present interest and are borrowed from those used for B_4C.

Recent research has demonstrated that the hexagonal (wurtzite) phase of SiC undergoes amorphization upon shock compression, commensurate with an increase in local mass density (Zhao et al., 2018). In contrast, β-SiC expands upon amorphization (Vashishta et al., 2007), so this structural change is not pertinent for compressive loading. A phase change from zinc blende to rock salt structure occurs at pressures at or in excess of 60 GPa (Vashishta et al., 2007) and is also irrelevant for the present more modest loading protocols where local pressures do not exceed 10 GPa. Hexagonal and cubic phases are both non-centrosymmetric semiconductors with weakly piezoelectric properties (Phillips and Van Vechten, 1969). Though of possible importance for defect mobility in single crystals (Clayton, 2010), electromechanical effects are deemed unimportant for brittle polycrystals with random orientations studied here. As was the case in §3, residual stresses, initial porosity, inclusions, and tertiary phases are deferred for consideration in future work.

4.2. Microstructure rendering and boundary conditions

Three microstructure morphologies are considered, as shown in Fig. 5. Techniques for mesh generation are discussed in Clayton and Knap (2015). The edge length of the cube-shaped polycrystalline domain Ω is $L = 10\,\mu$m, and the average grain size is $L/50^{1/3} \approx 2.5\,\mu$m. All microstructures contain 50 polyhedral grains, where as discussed in §3, the average grain size is $L/50^{1/3} \approx 2.5\,\mu$m. Let V_1 and V_2 denote volume fractions of diamond and SiC, respectively, where the latter ranges from 10% to 28%. In microstructures 1 and 3, a layer of uniform thickness (200 nm) of nanocrystalline SiC encapsulates each diamond crystal, contributing 20.3% by volume of phase 2. Microstructures 2 and 3 both contain five randomly oriented SiC crystals of micron dimensions. For each microstructure, two different distributions of random lattice orientations associated with ($\boldsymbol{S}$, $\boldsymbol{M}$, $\boldsymbol{N}$) are assigned to the 50 grains. A uniform lattice orientation is assigned to the nanocrystalline SiC layer in microstructures 1 and 3 since individual crystals are too small to be resolved by the FE mesh. In each case, a dominant {110}-type fracture plane (orientation $\boldsymbol{N}$) is set to coincide with a plane oriented at 45° to the direction of compressive loading, yielding the maximum resolved stress for shear fracture. Specifically, if loading is normal to [001], the active twinning system for ($\boldsymbol{S}$, $\boldsymbol{M}$) is $[11\bar{2}](111)$, and $\boldsymbol{N}$ is prescribed as (101) for orientation set 1 (close to $\boldsymbol{M}$) and $(0\bar{1}1)$ for orientation set 2 (far from $\boldsymbol{M}$). For each of the six cases (three microstructures × two orientation sets), one simulation is performed with twinning enabled in β-SiC using properties from Table 3. A second simulation for each case is performed with twinning shear suppressed, i.e., $\eta(\boldsymbol{X}) = 0 \forall \boldsymbol{X} \in \Omega$ is enforced. The total number of simulations reported in §4 becomes twelve, where fracture $[\xi(\boldsymbol{X}) > 0]$ is always enabled.

Boundary conditions resulting in an overall state of uniaxial compressive stress are applied. Free boundaries are prescribed with respect to order parameters ($r = s = 0$ on $\partial\Omega$). Details are identical to those of §3.

4.3. Finite element simulations and analysis of results

Results of the twelve FE simulations for diamond-SiC are now reported. Representative contours of η depicting twinning and associated stacking fault propagation in SiC crystals are shown in Fig. 6. Scale bars are quadratic to enable visualization of low levels of transformation ($0 \lesssim \eta \lesssim 0.25$), which occur primarily in preferentially oriented intergranular nanocrystalline layers and less so in larger bulk grains of SiC. Recall that the diamond grains, which can

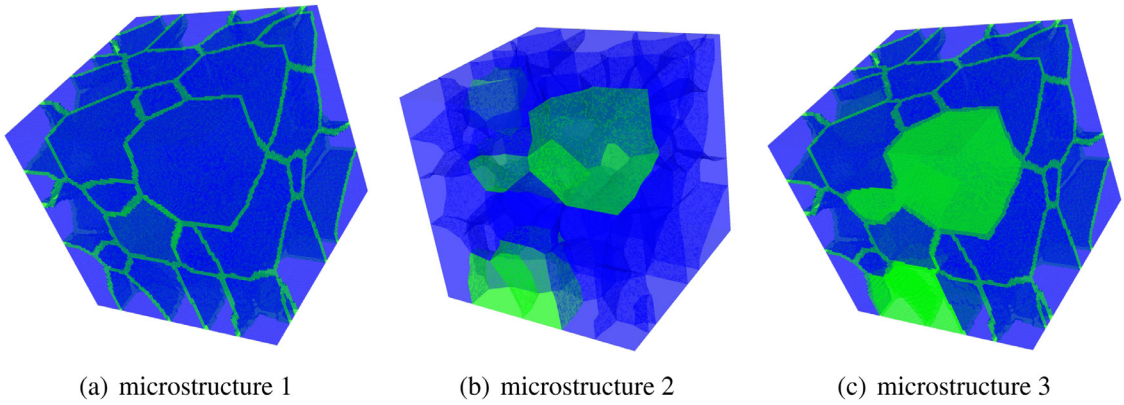


Fig. 5. Meshes for diamond-SiC; (C, SiC) crystals are (blue, green) and V_2 is the volume fraction of SiC: (a) microstructure 1, $V_2 = 0.20$ (b) microstructure 2, $V_2 = 0.10$ (c) microstructure 3, $V_2 = 0.28$.

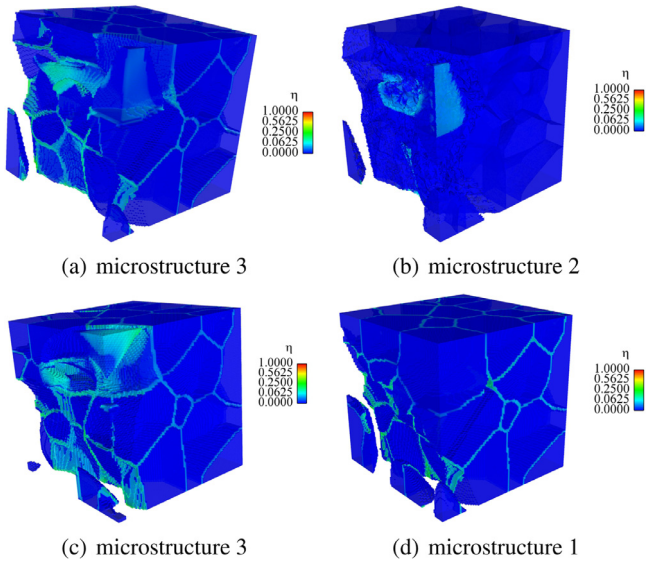


Fig. 6. Order parameter η contour for diamond-SiC at applied compressive strain $\bar{\epsilon} = 0.6\%$ with highly degraded elements ($\xi > 0.8$) visually removed to show fractures: (a) $V_2 = 0.28$, lattice 2 (b) $V_2 = 0.10$, lattice 2 (c) $V_2 = 0.28$, lattice 1 (d) $V_2 = 0.20$, lattice 2.

be identified using Fig. 5, do not undergo twinning or any other structural changes, i.e., $\eta = 0$ for all $\boldsymbol{X} \in$ phase 1. Fracture behaviors are qualitatively similar for most microstructures shown in Fig. 6, with damage in the form of crumbling and pulverization concentrated on the left front face of the cube of the aggregate ($\xi > 0.8$). This region is notably where more of the weaker bulk SiC grains are clustered for microstructures 2 and 3. Resistance to local fracture in the two ceramic crystal types can be inferred from values of Υ in Table 3, with a significantly larger value for diamond.

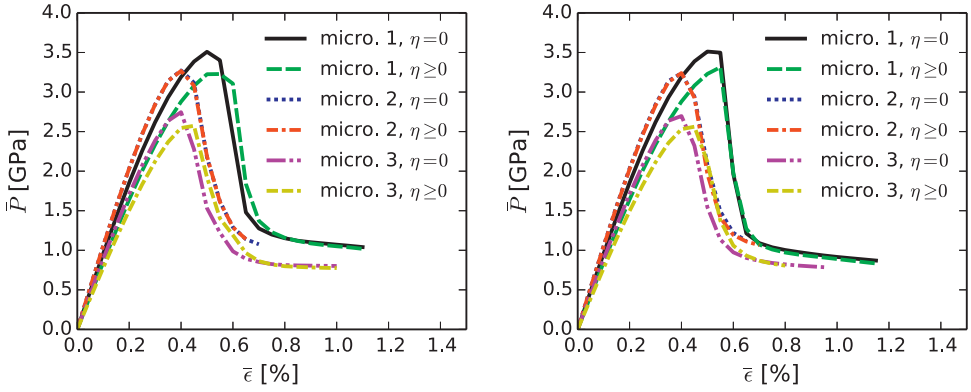
Fracture is less severe at the applied strain level shown ($\bar{\epsilon} = 0.6\%$) for the case in Fig. 6(d), which features intergranular layers of the more ductile SiC phase but no bulk SiC grains. In contrast, damage appears most severe for the case shown in Fig. 6(b), which contains bulk SiC crystals but no intergranular layers of nanocrystalline SiC. In this case, twinning manifests only in a few preferentially oriented grains. All cases demonstrate mixtures of intergranular and transgranular fractures. The fraction of grain boundary fractures is notably higher for the case shown in Fig. 6(c) than in Fig. 6(a), demonstrating effects of lattice orientation on damage morphology. Different regions of bulk SiC crystals in these two cases demonstrate non-negligible twinning ($\eta > 0$).

Notation follows that of §3 for volume averaged axial compressive stress and order parameters $\bar{P}$, $\bar{\eta}$, and $\bar{\xi}$. These quantities are shown versus applied axial compressive nominal strain $\bar{\epsilon}$ in Fig. 7. Average stresses for simulations featuring lattice orientation sets 1 and 2 are given in respective Fig. 7(a) and (b). Stiffer responses are obtained with structural transformations suppressed via $\eta = 0$ for microstructures 1 and 3 that contain integranular layers of SiC. Physically, more compliance results from deviatoric deformation accommodation from twinning when $\eta > 0$. Deformation twinning is too limited in microstructure 2 to affect its peak stresses and corresponding values of $\bar{\epsilon}_C$.

Trends in average results are similar for orientation sets 1 and 2, with minor differences evident only upon close comparison of like-labeled curves in Fig. 7(a) and (b). Maximum compressive stress $P_C = \max_{\bar{\epsilon}}(\bar{P})$ is largest for microstructure 1 (SiC at GB layers only), moderate for microstructure 2 (bulk SiC grains only), and smallest for microstructure 3 (SiC both in GB layers and bulk grains). Even though the volume fraction of the softer and weaker SiC phase is larger in microstructure 1 (around 20%) than microstructure 2 (around 8%), unconfined compressive strength is generally larger in microstructure 1. This result demonstrates that the morphology and lattice orientation of the second phase crucially affects overall strength of the composite. Ductility ϵ_C, which may be recalled as defined as the applied strain $\bar{\epsilon}$ corresponding to peak load P_C, follows the same general trends, although differences in values among microstructures 2 and 3 are small for cases wherein twinning is suppressed.

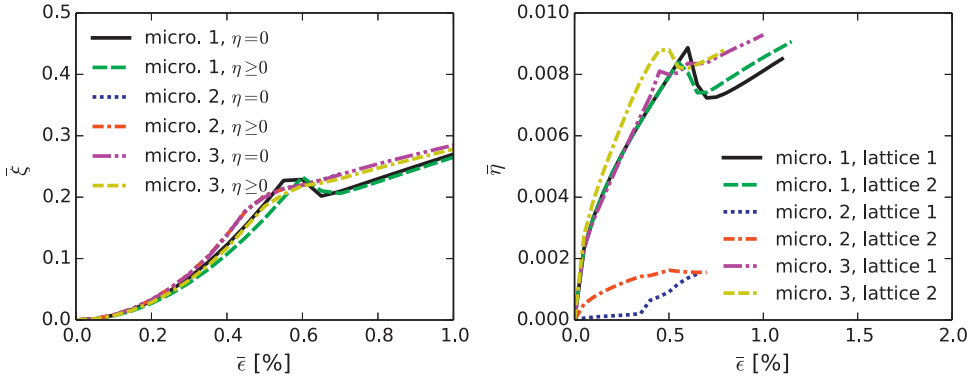
Average fracture order parameter $\bar{\xi}$ for orientation set 1 is shown in Fig. 8(a). Results are not shown for orientation set 2 since trends and magnitudes are similar. Average stress-strain and fracture behaviors relatively insensitive to orientation were similarly noted for different ceramic microstructures in §3 of this work and in Clayton and Knap (2018a,b). Microstructures 1 and 3 with $\eta = 0$ demonstrate the largest values of $\bar{\xi}$, though the former is among the stiffest cases in Fig. 7. The average damage parameter is not necessarily correlated with overall strength degradation; instead aggregate failure is associated with the formation of one or a few dominant cracks. Histories of $\bar{\xi}$ are not drastically different among the other cases shown in Fig. 8(a).

Average structure change $\bar{\eta}$ measuring twinning and stacking fault formation for all six simulations where transformations are enabled is shown in Fig. 8(b). Lattice orientation set 2 demonstrates significantly more transformation activity than lattice orientation set 1 for microstructures 2 and 3, with $\bar{\eta}$ for both orientations similar in microstructure 1. Microstructure 2, containing micron-sized bulk SiC grains but no nanocrystalline SiC layers at GBs, demonstrates far less structure change associated with



(a) lattice orientation set 1 (b) lattice orientation set 2

Fig. 7. Average axial stress $\bar{P}$ versus applied compressive strain $\bar{\epsilon}$ for diamond-SiC.



(a) lattice orientation set 1 (b) both orientation sets

Fig. 8. Average order parameters versus applied compressive strain $\bar{\epsilon}$ in diamond-SiC for (a) fracture $\bar{\xi}$ (b) twinning $\bar{\eta}$.

Table 4
Peak compressive stress (P_C), associated strain (ϵ_C), and averaged order parameters (ξ_C, η_C) for C-SiC composites.

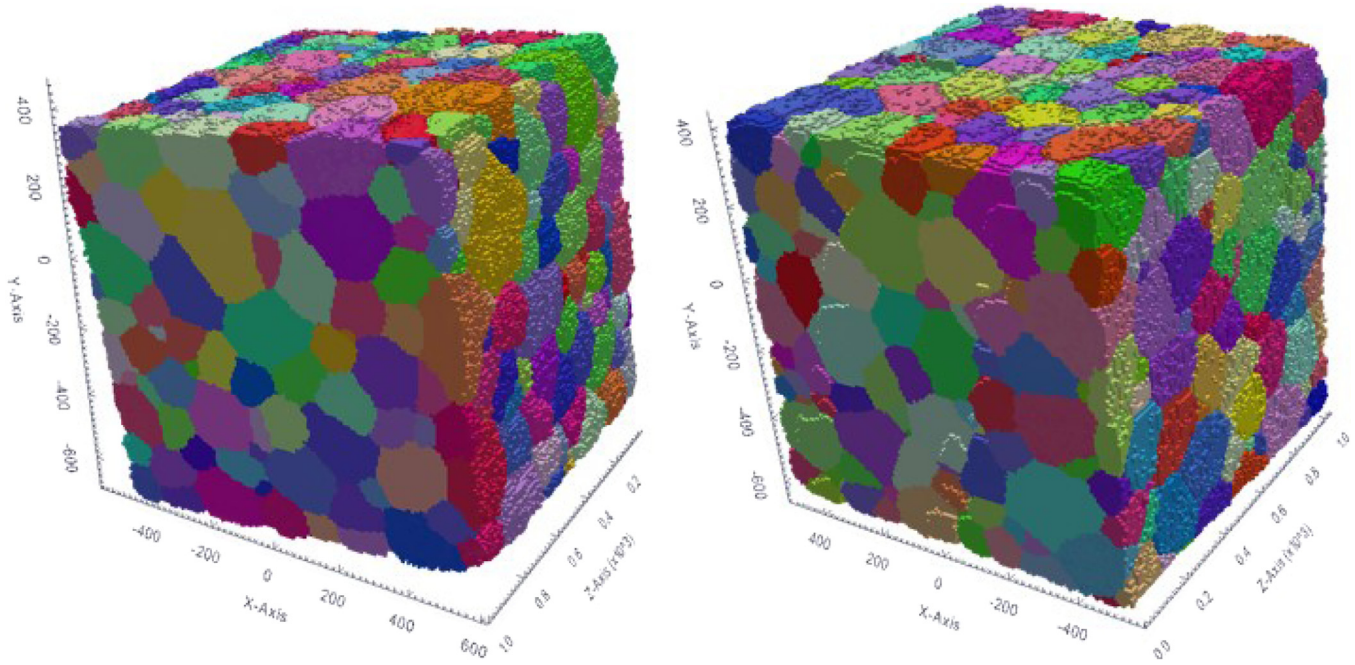
Microstructure (fraction SiC)	Lattice orientation	Slip/twins active	P_C [GPa]	ϵ_C [%]	ξ_C	η_C
1 ($V_2 = 0.20$)	1	N	3.51	0.50	0.189	–
	1	Y	3.23	0.55	0.199	0.0084
	2	N	3.51	0.50	0.189	–
	2	Y	3.31	0.55	0.199	0.0084
2 ($V_2 = 0.10$)	1	N	3.27	0.40	0.139	–
	1	Y	3.27	0.40	0.139	0.0006
	2	N	3.24	0.40	0.140	–
	2	Y	3.24	0.40	0.138	0.0014
3 ($V_2 = 0.28$)	1	N	2.74	0.40	0.137	–
	1	Y	2.57	0.45	0.151	0.0081
	2	N	2.70	0.40	0.139	–
	2	Y	2.56	0.45	0.149	0.0084

$\bar{\eta}$ than microstructures 1 and 3 that contain larger volume fractions of SiC with effective habit planes preferentially oriented for twinning. This observation is consistent with contours of Fig. 6 that show little twinning activity in bulk grains of the SiC phase relative to more profuse, but incomplete ($0 < \eta < \eta_0$), twinning transformations in the GB layers.

Average data on peak stress, ductility/strain, and order parameters are given in Table 4. In microstructure 1, unconfined compressive strength P_C is around 3.5 GPa for cases with twinning deactivated and around 3.3 GPa for cases with $\eta > 0$ enabled. In microstructure 2, analogous values are 3.3 and 3.2; in microstructure 3, 2.7 and 2.6 (all in units of GPa). Static unconfined compressive strength has not been measured experimentally for this particular ceramic composite, to the authors' knowledge. Pure cubic SiC grown by CVD has demonstrated compressive strength in excess of 8 GPa, albeit in highly textured micro-pillar specimens of much smaller sizes (Shin et al., 2012).

Comparing values for microstructures 1 and 3 peak stress P_C decreases with increasing V_2 regardless of whether slip/twinning is disabled. Addition of bulk SiC grains to polycrystalline diamond decreases overall compressive strength of the composite. Ductility is likewise reduced with increasing V_2 in these cases, as is also evident from Fig. 7. When inelastic deformation mechanisms are enabled via $\eta > 0$, then twins and stacking faults in SiC, predominantly in GB layers, in microstructures 1 and 3 provide a slight increase in ductility as measured by ϵ_C. Ductility is lowest for microstructure 2, which does not contain nanocrystalline SiC layers at GBs. As mentioned already, strength P_C is also lower for microstructure 2 than microstructure 1, though the latter contains twice as much SiC by volume fraction. Distributed damage as measured by ξ_C increases modestly when slip/twins are enabled in microstructures 1 and 3. This is opposite to the trend observed for B_4C-TiB_2 in §3.

Experimental data (Zhao et al., 2004) show that fracture toughness of polycrystalline diamond may be improved by addition of intergranular SiC layers, with the enhancement increasing with decreasing size of the SiC grains down to grain diameters on the order of tens of nm. The present results are in qualitative agreement, showing improved unconfined compressive strength in samples with nanocrystalline GB layers relative to those with micro-crystalline bulk SiC grains. Residual stresses may arise during thermal processing. These are thought to be substantial and



(a) AlON sample 1 (b) AlON sample 2

Fig. 9. Digital renderings of polycrystals generated using DREAM.3D package (Groeber and Jackson, 2014): (a) 620 grains (b) 660 grains.

compressive in the diamond phase and tensile in the SiC phase (Liu et al., 2015). Such stresses would inhibit cleavage in the diamond but might promote failure of the SiC. Phase boundaries may increase toughness by deflecting cleavage cracks in the stiffer diamond phase, behavior which is observed in some of the present simulations. However, while preferred intergranular fracture is observed between phases in Fig. 6(c), overall compressive strength is in this instance improved very little relative to the case shown in Fig. 6(a).

Future work should consider residual stresses, more microstructures, and more orientation distributions. Also of possible importance are elastic anisotropy and nonlinearity, tertiary phases, initial porosity, and multiple twin and/or cleavage systems per crystal. Effects of chemistry and orientation on intergranular and interphase properties should be investigated. As remarked in §3, simultaneous consideration of all possible mechanisms is presently prohibited by computational cost. With regard to material design, the present results, with stated limitations, imply the following. Firstly, compressive strength is improved by efforts that inhibit cleavage fracture in bulk grains of either phase, notably by addition of nanocrystalline layers of SiC along GBs. Secondly, promotion of twinning in the SiC phase may improve ductility but reduce peak strength. Finally, effects of lattice orientation on overall average strength and ductility appear secondary to effects of phase morphology and volume fraction, though inferences could change if additional physical mechanisms are incorporated in the model.

As also mentioned in §3, microstructures of larger domain sizes with far more grains should be considered in order to obtain homogenized responses more statistically representative of macroscopic behavior. These larger domains should enable studies of interactions of longer cracks with grain and phase boundaries and may be sufficient to quantify toughening mechanisms such as crack bridging and crack deflection by secondary phases.

Representative digital microstructures of larger polycrystalline aggregates for FE meshing may be imported or designed from appropriate characterization data using the DREAM.3D software (Groeber and Jackson, 2014). Shown in Fig. 9 are two such microstructures for ceramic polycrystals. Images in Fig. 9(a) and (b) correspond to single phase microstructures with 620 and 660 grains, respectively. Specifically, these two images are 3D reconstructions produced in DREAM.3D of aluminum oxynitride (AlON), a transparent ceramic studied in Clayton (2011a), Clayton et al. (2012), and Leavy et al. (2013), from real one-mm cubes of the material. Grain orientations and geometry were obtained using high-energy X-ray diffraction microscopy (HEDM) at the dynamic compression sector (DCS) of the advanced photon source (APS), in collaboration with B. Suter and S. Maddali of Carnegie Mellon University. Statistics were extracted for synthetic mesh generation in DREAM.3D.

Future work will invoke phase field methods advanced in the present paper towards larger polycrystalline and polyphase systems, perhaps using explicit time integration techniques for order parameter evolution. Such techniques may prove more computationally efficient than conjugate gradient energy minimization, particularly in globally strain-softening regimes.

5. Conclusions

A phase field framework has been developed to model elasticity, inelasticity, and fracture in ceramic composites. Inelastic modes include partial slip, twinning, and stress-induced amorphization. Finite element simulations of unconfined compression have been undertaken for two ceramics: B_4C-TiB_2 and diamond-SiC. In both systems, fractures are found energetically favorable over other inelastic modes that are active to a limited extent and only in preferentially oriented grains.

Results for B_4C-TiB_2 suggest that the less brittle TiB_2 phase can inhibit cleavage fractures in the composite and that suppression of localized inelastic deformation modes in B_4C improves overall strength and ductility. Improvements are relatively modest however, suggesting that initial residual stresses and larger domain sizes should be considered in future modeling to realize improvements commensurate with experimental measurements of fracture toughness. Results for diamond-SiC suggest that incorporation of the softer SiC phase in nanocrystalline layers along grain

boundaries enhances overall strength and ductility relative to microstructures with less SiC in the form of larger grains. Activation of twinning in the SiC layers may improve ductility of the composite, though peak strength may be compromised. Overall peak unconfined compressive strength is larger for diamond-SiC (up to 3.5 GPa) than B_4C-TiB_2 (up to 2.1 GPa), while strain at peak loading indicative of ductility follows the opposite trend (up to 0.55% for diamond-SiC, 0.7% for B_4C-TiB_2).

Acknowledgments

JDC and RBL acknowledge support from ARL-WMRD 6.1 FY19+ programs on *Mesoscale Modeling of Heterogeneous Polycrystals* and *Hierarchical Diamond-based Ceramic Composites*. Prof. Jincheng Du of the University of North Texas is thanked for providing values of fracture surface energy and stacking fault energy for basal slip in TiB_2 prior to formal publication. Prof. Tom Scharf of the University of North Texas is thanked for providing technical background on B_4C-TiB_2 composites. Dr. Shawn Coleman of ARL is thanked for providing technical background and a literature database on diamond-SiC composites.

Supplementary material

Supplementary material associated with this article can be found, in the online version, at doi:10.1016/j.ijsolstr.2019.02.016.

References

An, Q., Goddard, W., 2015. Atomistic origin of brittle failure of boron carbide from large-scale reactive dynamics simulations: suggestions toward improved ductility. Phys. Rev. Lett. 115, 105051.
An, Q., Goddard, W.A., Cheng, T., 2014. Atomistic explanation of shear-induced amorphous band formation in boron carbide. Phys. Rev. Lett. 113, 095501.
Bammann, D., Solanki, K., 2010. On kinematic, thermodynamic, and kinetic coupling of a damage theory for polycrystalline material. Int. J. Plast. 26, 775–793.
Bardenhagen, S., Nairn, J.A., Lu, H., 2011. Simulation of dynamic fracture with the material point method using a mixed J-integral and cohesive law approach. Int. J. Fract. 170, 49–66.
Beaudet, T., Smith, J., Adams, J., 2015. Surface energy and relaxation in boron carbide $(10\bar{1}1)$ from first principles. Solid State Commun 219, 43–47.
Biswas, S., Schwen, D., Singh, J., Tomar, V., 2016. A study of the evolution of microstructure and consolidation kinetics during sintering using a phase field modeling based approach. Extreme Mech Lett 7, 78–89.
Biswas, S., Schwen, D., Wang, H., Okuniewski, M., Tomar, V., 2018. Phase field modeling of sintering: role of grain orientation and anisotropic properties. Comput. Mater. Sci 148, 307–319.
Borden, M., Verhoosel, C., Scott, M., Hughes, T., Landis, C., 2012. A phase-field description of dynamic brittle fracture. Comput. Methods Appl. Mech. Eng. 217, 77–95.
Chen, M., McCauley, J., Hemker, K., 2003. Shock-induced localized amorphization in boron carbide. Science 299, 1563–1566.
Christian, J., Mahajan, S., 1995. Deformation twinning. Prog. Mater. Sci. 39, 1–157.
Clayton, J., 2005. Dynamic plasticity and fracture in high density polycrystals: constitutive modeling and numerical simulation. J. Mech. Phys. Solids 53, 261–301.
Clayton, J., 2010. Modeling nonlinear electromechanical behavior of shocked silicon carbide. J. Appl. Phys. 107, 013520.
Clayton, J., 2011a. A nonlinear thermomechanical model of spinel ceramics applied to aluminum oxynitride (alon). J. Appl. Mech. 78, 011013.
Clayton, J., 2011b. Nonlinear Mechanics of Crystals. Springer, Dordrecht.
Clayton, J., 2012. Towards a nonlinear elastic representation of finite compression and instability of boron carbide ceramic. Philos. Mag. 92, 2860–2893.
Clayton, J., 2014a. Finite strain analysis of shock compression of brittle solids applied to titanium diboride. Int. J. Impact Eng. 73, 56–65.
Clayton, J., 2014b. Phase field theory and analysis of pressure-shear induced amorphization and failure in boron carbide ceramic. AIMS Mater. Sci. 1, 143–158.
Clayton, J., 2016. Finsler-geometric continuum mechanics and the micromechanics of fracture in crystals. J. Micromech. Mol. Phys. 1, 1640003.
Clayton, J., 2017a. Finser-geometric continuum dynamics and shock compression. Int. J. Fract. 208, 53–78.
Clayton, J., 2017b. Finsler geometry of nonlinear elastic solids with internal structure. J. Geom. Phys. 112, 118–146.
Clayton, J., 2017c. Generalized finsler geometric continuum physics with applications in fracture and phase transformations. Zeitschrift fur Angewandte Mathematik und Physik (ZAMP) 68, 9.
Clayton, J., 2018. Shock compression of metal single crystals modeled via finsler-geometric continuum theory. AIP Conf. Proc. 1979, 180001.
Clayton, J., Knap, J., 2011a. A phase field model of deformation twinning: nonlinear theory and numerical simulations. Phys. D 240, 841–858.
Clayton, J., Knap, J., 2011b. Phase field modeling of twinning in indentation of transparent single crystals. Modell. Simul. Mater. Sci. Eng. 19, 085005.
Clayton, J., Knap, J., 2013. Phase field analysis of fracture induced twinning in single crystals. Acta Mater. 61, 5341–5353.
Clayton, J., Knap, J., 2014. A geometrically nonlinear phase field theory of brittle fracture. Int. J. Fract. 189, 139–148.
Clayton, J., Knap, J., 2015. Phase field modeling of directional fracture in anisotropic polycrystals. Comput. Mater. Sci 98, 158–169.
Clayton, J., Knap, J., 2016. Phase field modeling of coupled fracture and twinning in single crystals and polycrystals. Comput. Methods Appl. Mech. Eng. 312, 447–467.
Clayton, J., Knap, J., 2018a. Continuum modeling of twinning, amorphization, and fracture: theory and numerical simulations. Continuum. Mech. Thermodyn. 30, 421–455.
Clayton, J., Knap, J., 2018b. Geometric micromechanical modeling of structure changes, fracture, and grain boundary layers in polycrystals. J. Micromech. Mol. Phys. 3, 1840001.
Clayton, J., Kraft, R., Leavy, R., 2012. Mesoscale modeling of nonlinear elasticity and fracture in ceramic polycrystals under dynamic shear and compression. Int. J. Solids Struct. 49, 2686–2702.
Clayton, J., Tonge, A., 2015. A nonlinear anisotropic elastic-inelastic constitutive model for polycrystalline ceramics and minerals with application to boron carbide. Int. J. Solids Struct. 64–65, 191–207.
Coleman, S., Hernandez-Rivera, E., Behler, K., Synowczynski-Dunn, J., Tschopp, M., 2016. Challenges of engineering grain boundaries in boron-based armor ceramics. JOM 68, 1605–1615.
Dandekar, D., Benfanti, D., 1993. Strength of titanium diboride under shock wave loading. J. Appl. Phys. 73 (2), 673–679.
Demirskyi, D., Borodianska, H., Sakka, Y., Vasylkiv, O., 2017. Ultra-high elevated temperature strength of TiB_2-based ceramics consolidated by spark plasma sintering. J. Eur. Ceram. Soc. 37, 393–397.
Du, J., Chen, R., 2018. First principles calculations of interfacial structures and impact on mechanical properties in armor ceramics. Technical Report, W911NF-16-2-0189. University of North Texas, Denton, TX.
Erhart, P., Albe, K., 2005. Analytical potential for atomistic simulations of silicon, carbon, and silicon carbide. Phys. Rev. B 71, 035211.
Espinosa, H., 1995. On the dynamic shear resistance of ceramic composites and its dependence on applied multiaxial deformation. Int. J. Solids Struct. 32, 3105–3128.
Fanchini, G., McCauley, J., Chhowalla, M., 2006. Behavior of disordered boron carbide under stress. Phys. Rev. Lett. 97, 035502.
Field, J., 2012. The mechanical and strength properties of diamond. Rep. Prog. Phys. 75, 126505.
Grady, D., 2011. Adiabatic shear failure in brittle solids. Int. J. Impact Eng. 38, 661–667.
Groeber, M., Jackson, M., 2014. DREAM.3D: a digital representation environment for the analysis of microstructure in 3D. Integrat. Mater. Manuf. Innovat. 3, 5.
Han, Y., Tomar, V., 2016. An investigation into the influence of grain boundary misorientation on the tensile strength of SiC bicrystals. Mech. Adv. Mater. Struct. 23, 494–502.
Kikuchi, H., Kalia, R., Nakano, A., Vashishta, P., Branicio, P., Shimojo, F., 2005. Brittle dynamic fracture of crystalline cubic silicon carbide (3C-Sic) via molecular dynamics simulation. J. Appl. Phys. 98, 103524.
Kohyama, M., 1999. Tensile strength and fracture of a tilt grain boundary in cubic SiC: a first-principles study. Philos. Mag. Lett. 79, 659–672.
Leavy, R., Clayton, J., Strack, O., Brannon, R., Strassburger, E., 2013. Edge on Impact Simulations and Experiments. In: Procedia Engineering, 58. Elsevier, pp. 445–452.
Levin, V., Levitas, V., Zingerman, K., Freiman, E., 2013. Phase-field simulation of stress-induced martensitic phase transformations at large strains. Int. J. Solids Struct. 50, 2914–2928.
Levitas, V., 2014. Phase field approach to martensitic phase transformations with large strains and interface stresses. J. Mech. Phys. Solids 70, 154–189.
Levitas, V., Levin, V., Zingerman, K., Freiman, E., 2009. Displacive phase transitions at large strains: phase-field theory and simulations. Phys. Rev. Lett. 103, 025702.
Li, Y., Zhao, Y., Liu, W., Zhang, Z., Vogt, R., Lavernia, E., Schoenung, J., 2010. Deformation twinning in boron carbide particles within nanostructured al 5083/b_4c metal matrix composites. Philos. Mag. 90, 783–792.
Liu, Y., Hu, C., Feng, W., Men, J., Cheng, L., Zhang, L., 2014. Microstructure and properties of diamond/SiC composites prepared by tape-casting and chemical vapor infiltration process. J. Eur. Ceram. Soc. 34, 3489–3498.
Liu, Y., Hu, C., Men, J., Feng, W., Cheng, L., Zhang, L., 2015. Effect of diamond content on microstructure and properties of diamond/SiC composites prepared by tape-casting and CVI process. J. Eur. Ceram. Soc. 35, 2233–2242.
Matthey, B., Höhn, S., Wolfrum, A.-K., Mühle, U., Motylenko, M., Rafaja, D., Michaelis, A., Herrmann, M., 2017. Microstructural investigation of diamond-Sic composites produced by pressureless silicon infiltration. J. Eur. Ceram. Soc. 37, 1917–1928.
Ning, X., Ye, H., 1990. Experimental determination of the intrinsic stacking-fault energy of SiC crystals. J. Phys. 2, 10223–10225.
Phillips, J., Van Vechten, J., 1969. Charge redistribution and piezoelectric constants. Phys. Rev. Lett. 23, 1115–1117.
Reddy, K., Guo, J., Shinoda, Y., Fujita, T., Hirata, A., Singh, J., McCauley, J., Chen, M.,

2012. Enhanced mechanical properties of nanocrystalline boron carbide by nanoporosity and interface phases. Nat. Commun. 3, 1052.
Rice, J., 1968. Mathematical analysis in the mechanics of fracture. In: Liebowitz, H. (Ed.), Fracture: An Advanced Treatise. Academic Press, New York, pp. 191–311.
Scharf, T., Rubink, W., 2018. Development of high strength, high toughness B_4C-based composites. Technical Report, W911NF-16-2-0189. University of North Texas, Denton, TX.
Shin, C., Jin, H.-H., Kim, W.-J., Park, J.-Y., 2012. Mechanical properties and deformation of cubic silicon carbide micropillars in compression at room temperature. J. Am. Ceram. Soc. 95, 2944–2950.
Sigl, L., Kleebe, H.-J., 1995. Microcracking in b_4C-Tib_2 composites. J. Am. Ceram. Soc. 78, 2374–2380.
Tomar, V., 2008. Analyses of the role of grain boundaries in mesoscale dynamic fracture resistance of SiC-Si_3n_4 intergranular nanocomposites. Eng. Fract. Mech. 75, 4501–4512.
Tomar, V., Zhai, J., Zhou, M., 2004. Bounds for element size in a variable stiffness cohesive finite element model. Int. J. Numer. Methods Eng. 61, 1894–1920.
Van Torne, L., 1966. Twinning in β–silicon carbide. Phys. Status Solidi B 14, K123–K126.
Vanderwalker, D., Croft, W., 1988. Dislocations in shock-loaded titanium diboride. J. Mater. Res. 3, 761–763.
Vashishta, P., Kalia, R., Nakano, A., Rino, J.P., 2007. Interaction potential for silicon carbide: a molecular dynamics study of elastic constants and vibrational density of states for crystalline and amorphous silicon carbide. J. Appl. Phys. 101, 103515.
Verma, D., Biswas, S., Prakash, C., Tomar, V., 2017. Relating interface evolution to interface mechanics based on interface properties. JOM 69, 30–38.
White, R., Dickey, E., 2011. The effects of residual stress distributions on indentation-induced microcracking in b_4C–Tib_2 eutectic ceramic composites. J. Am. Ceram. Soc. 94, 4032–4039.
Xu, X.-P., Needleman, A., 1994. Numerical simulations of fast crack growth in brittle solids. J. Mech. Phys. Solids 42, 1397–1434.
Yan, X., Tang, Z., Zhang, L., Guo, J., Jin, C., Zhang, Y., Goto, T., McCauley, J., Chen, M., 2009. Depressurization amorphization of single-crystal boron carbide. Phys. Rev. Lett. 102, 075505.
Yang, Z., He, X., Wu, M., 2013. Fabrication of diamond/SiC composites by si-vapor vacuum reactive infiltration. Ceram. Int. 39, 3399–3403.
Zhao, S., Flanagan, R., Hahn, E., Kad, B., Remington, B., Wehrenberg, C., Cauble, R., More, K., Meyers, M., 2018. Shock-induced amorphization in silicon carbide. Acta Mater. 158, 206–213.
Zhao, Y., Qian, J., Daemen, L., Pantea, C., Zhang, J., Voronin, G., Zerda, T., 2004. Enhancement of fracture toughness in nanostructured diamond–Sic composites. Appl. Phys. Lett. 84, 1356–1358.